

RESEARCH ARTICLE

How a table modulates the risk of airborne transmission between facing individuals

Oğuzhan Kaplan^{1,3}, Manouk Abkarian² and Simon Mendez ¹

¹Institut Montpelliérain Alexander Grothendieck, CNRS, University of Montpellier, Montpellier, France

²Centre de Biologie Structurale, Université de Montpellier, CNRS UMR 5048, INSERM UMR 1054, Montpellier, France

³CORIA-UMR6614, Normandie Université, CNRS, INSA et Université de Rouen, Avenue de l'Université,

Saint-Etienne-du-Rouvray, France

Corresponding author: Simon Mendez; Email: simon.mendez@umontpellier.fr

Received: 26 November 2024; Revised: 4 September 2025; Accepted: 7 September 2025

Keywords: disease transmission; numerical simulations; respiratory flows

Abstract

Airborne transmission has been recognised as an important route of transmission for SARS-CoV-2, the virus responsible for the COVID-19 pandemic. While coughing and sneezing are major aerosol sources, asymptomatic transmission highlights the need to study other exhalation modes in social settings. Gathering around a table, a common scenario for human interactions, may influence airborne transmission by modifying the airflows. Here, we employ high-fidelity large-eddy simulations to investigate the effect of a table for periodic breathing conditions (Reynolds number $Re \approx 10^3 - 3 \times 10^3$, Froude number $Fr \approx 17-50$) as well as during sudden, forceful exhalations at peak values of $Re \approx 1.2 \times 10^4$ and $Fr \approx 70$, mimicking laughter. During downward exhalations, the distance between the source and the table defines a new length scale that constrains the natural spread of buoyant puffs and jets. The table limits forward particle transport but, in doing so, may increase particle concentrations reaching a recipient, raising transmission risks. Simulations of forceful exhalations, such as laughter, further show that the table acts as an inertial filter – intercepting medium-sized particles that would otherwise remain airborne. This introduces a cutoff size dependent on puff inertia, altering the resulting airborne particle size distribution.

Impact Statement

Human expiratory flows have been under a research spotlight since the onset of the SARS-CoV-2 pandemic, owing to their crucial role in airborne transmission of respiratory viruses. Using flow simulations, we demonstrate how a table located between two people modulates exhaled flows and the transport of exhaled virus-laden droplets. For the first time, we propose a panorama of physical phenomena that modify the flow and the transmission risk in a conversation at a table: the table limits forward transport of airborne pathogens, concentrates them in the air but also collects the largest droplets due to inertial impact. All of these effects stress the relevance of accounting for the geometry of the environment when assessing transmission risks of airborne diseases.

1. Introduction

Approximately five years after the onset of the Coronavirus disease 2019 (COVID-19) pandemic, caused by the severe acute respiratory syndrome coronavirus 2 (SARS-CoV-2), the time for emergency is over. On 5 May 2023, the World Health Organization had considered that COVID-19 no longer constituted a



public health emergency of international concern and issued recommendations for the long-term management of the disease (WHO, 2023). Nevertheless, the terrible human and economic costs of the pandemic, and the possible emergence of similar viruses or new variants of SARS-CoV-2 (Carabelli *et al.*, 2023), constitute formidable motivations to elucidate the biological, physical and social mechanisms at play in the transmission of such a disease as well as in its mitigation (Wang *et al.*, 2021*a,b*; Galasso *et al.*, 2020; Zhang *et al.*, 2020; Crunfli *et al.*, 2022; Howard *et al.*, 2021; Baxter-King *et al.*, 2022). In particular, the question of how microenvironments modulate the transmission risks remains acute (Nielsen & Xu, 2022) to define relevant public policies.

In airborne transmission of respiratory diseases, susceptible people get infected after inhaling viruses contained in particles suspended in the air, previously emitted by an infected individual (Morawska & Cao, 2020; Balachandar *et al.*, 2020; Wang *et al.*, 2021*a*; Bourouiba, 2021). These respiratory droplets are emitted during all expiratory activities, with their number and size distribution depending on the activity and on interindividual factors (Duguid, 1946; Johnson *et al.*, 2011; Gandhi *et al.*, 2020; Wells, 1934; Asadi *et al.*, 2020; Edwards *et al.*, 2021; Bagheri *et al.*, 2023). After their emission, the size of the particles evolves in the air due to the evaporation of their water content (Netz & Eaton, 2020). While leaving the mouth and/or the nose, they are accompanied by a mass of warm, humid air. The associated buoyant and turbulent flows modulate the transport of pathogen-laden particles in two principal ways: first, compared with isolated droplets, the settling time of suspended droplets is increased due to their entrapment in turbulent flow (Bourouiba *et al.*, 2014). Second, their evaporation is delayed, as the warm, humid expiratory air creates a buffer between the suspended droplets and the often colder, drier environment (Bourouiba, 2021; Chong *et al.*, 2021).

Many studies have been dedicated to coughing and sneezing puff flows from symptomatic individuals (Gupta *et al.*, 2009; Bourouiba *et al.*, 2014; Chong *et al.*, 2021; Bourouiba, 2021).

However, the importance of presymptomatic, paucisymptomatic and asymptomatic transmissions of COVID-19 (Oran & Topol, 2020) has highlighted that expiratory modes such as breathing and speech had been overlooked (Stadnytskyi *et al.*, 2020; Shao *et al.*, 2021; Abkarian *et al.*, 2020; Giri *et al.*, 2022; Singhal *et al.*, 2022; Cortellessa *et al.*, 2021; Faleiros *et al.*, 2022). From the flow point of view, breathing and speaking are characterised by successive puffs that may coalesce to form jet-like flows in the far field (Abkarian *et al.*, 2020; Giri *et al.*, 2022; Singhal *et al.*, 2022). In addition, flow rates, mouth positions and flow directions vary during speech (Abkarian *et al.*, 2020; Abkarian & Stone, 2020), possibly generating upward, forward and downward puffs, so that the knowledge gathered for coughs and sneezes is not directly transferable to speech (Abkarian *et al.*, 2020; Tang *et al.*, 2011).

Superspreading events in indoor settings (Miller *et al.*, 2021; Azimi *et al.*, 2021) have shed light on the long-range airborne transmission of SARS-CoV-2, for which exposure times and air renewal rates are critical (Bazant & Bush, 2021; Morawska & Cao, 2020; Bhagat *et al.*, 2020). On the other hand, in everyday conversations, people may keep a short distance from each other, which significantly reduces the time and length scales relevant to the airborne transmission. In such 'short-range' situations, the fine details of the expiratory air flows and droplet transport are crucial (Wang *et al.*, 2021*a*; Nielsen & Xu, 2022), which has for instance motivated the study of temperature and ambient air current effects (Mendez *et al.*, 2023; Wang *et al.*, 2021*c*).

However, case-control studies have shown that frequenting places that offer on-site eating and drinking are risk factors for contracting COVID-19 (Fisher *et al.*, 2020; Galmiche *et al.*, 2021). Indeed, in restaurants, bars and coffee shops for instance, people sit unmasked around a table, which naturally imposes a typical separation of approximately one metre. These situations are often prolonged, which increases the risk of disease transmission. The table is a surface on which the largest emitted droplets may deposit (Ding *et al.*, 2022), but it also modifies the air flows directed downwards, such as nose breathing or laughing flows (Bhagat *et al.*, 2020) (see experimental illustrations in movies S1–S3) and some speech-associated puffs (like 'ka' or 'ta' (Abkarian & Stone, 2020) or in words ending with a 't', such as 'light', for instance). Despite the interest of the table configuration for COVID-19 transmission, specific studies are rare and do not detail the flow–table interaction (Ding *et al.*, 2022; Faleiros *et al.*, 2022). In particular, does the presence of a table promote or inhibit the forward propagation

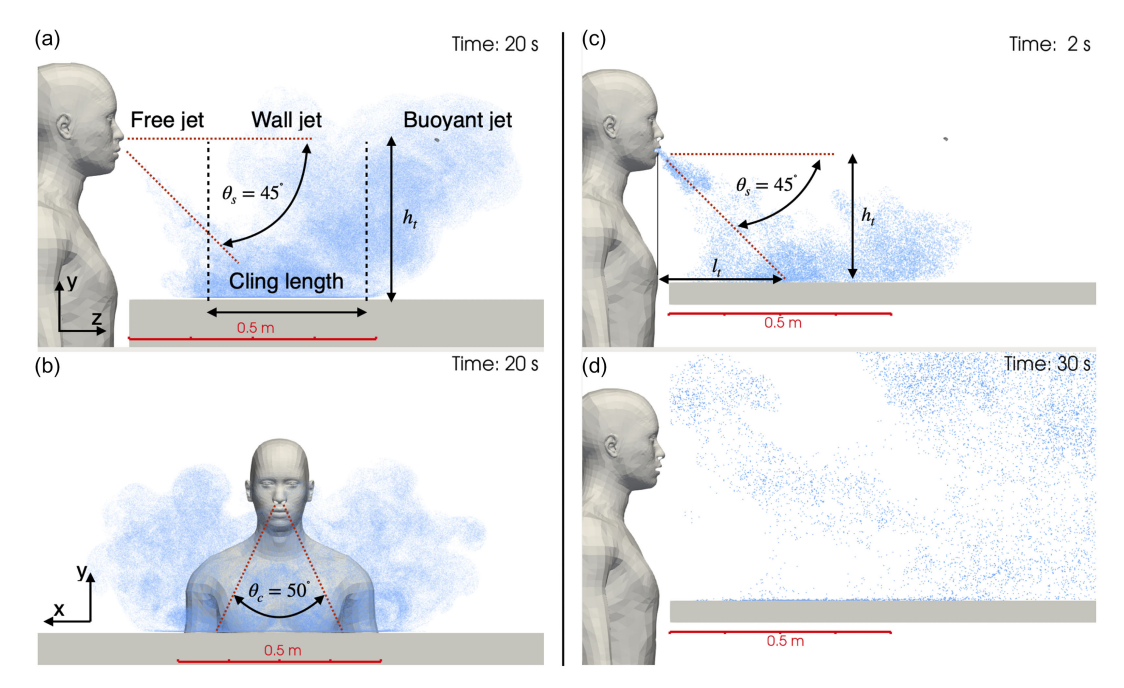


Figure 1. Numerical simulations of expiratory flows considered in the study: (a,b) side and front views of the breathing cloud generated after 5 cycles of periodic nasal breathing (t=20 s), for a 15 l min⁻¹ flow rate and a vertical height between the nostril exits and the table of $h_t = 32 \text{ cm}$. Typical values of orientation of nose breathing jets (Gupta et al., 2010) are imposed at the nostrils. (c,d) Two snapshots of laughing flow in front of a table at t=2 s (end of the injection signal) and t=30 s, respectively. A 45° downward orientation is imposed. Particles are single coloured. Note the large structures at the head of the jets, similar to observations from Sharp & Vyas (1977) and Burridge & Hunt (2017). The flow direction, impact on the table, clinging, lateral spreading in nose breathing are qualitatively illustrated in experimental supplementary movies S1, S2 (nose breathing) and S3 (laughing).

of respiratory particles? How does the table affect particles of different sizes, and what is its impact on the concentration of infectious aerosols reaching someone seated opposite an infected individual? These questions depart from the traditional motivations for studying oblique impinging jets, typically framed in cooling applications to maximise heat transfer (Goldstein & Franchett, 1988; Mishra *et al.*, 2020, 2023) or in vehicle take-off and landing scenarios (Nguyen *et al.*, 2020), where flow regimes differ markedly (e.g. higher Reynolds numbers, smaller nozzle-to-plate distances, isothermal conditions, steady jets). Consequently, dedicated investigations are required to address these questions.

In this paper, we use numerical simulations of expiratory flows to explore those open questions. Focus is placed on two configurations, chosen to mimic archetypes of expiratory flows: nose breathing, in which periodic exhalations coalesce to form a jet interacting with the table, and laughter, with a sudden series of air expulsions forming a puff impacting on the table, which is also a model for coughs or strong speech flows, such as plosion utterances. The scenarios are illustrated in figure 1.

The paper is organised as follows. Section 2 presents the flow simulations performed for this study. In §§ 3 and 4, we document breathing and laughing flows and their interaction with a table positioned horizontally below the emitter, and its consequence for the transport of emitted droplets. Section 5 summarises the key findings and discuss their broader implications.

2. Large-eddy simulations of respiratory flows

In order to provide the reader with an overview of the model and method used in this paper, the numerical simulations are briefly presented in this section. A thorough description is available in the Supplementary Materials.

2.1. Model and numerics

The numerical database of expiratory flows and aqueous droplets presented in the paper was generated through high-fidelity large-eddy simulations (LES) of the variable-density Navier–Stokes equations in the low-Mach regime using the in-house flow solver YALES2, previously employed in the airborne transmission context (Abkarian *et al.*, 2020; Yang *et al.*, 2020; Mendez *et al.*, 2023) (see other examples of LES in this context by Wang *et al.* (2021c) and Trivedi *et al.* (2021)). The unresolved sub-grid scale (SGS) stress tensor is modelled using the Boussinesq assumption with the so-called σ -model (Nicoud *et al.*, 2011) for the sub-grid turbulent viscosity. The σ -model has been built to yield zero SGS viscosity in situations where the flow is laminar, so that it is notably well adapted to moderate Reynolds numbers (Baya Toda *et al.*, 2014; Nicoud *et al.*, 2018; Zmijanovic *et al.*, 2017). The variable-density formulation allows us to account for thermal effects which are crucial to determine the dynamics of the exhaled cloud and for the evaporation of the droplets (Boulet *et al.*, 2018).

The solver uses the projection method, initially introduced by Chorin (1968) and subsequently modified by Kim & Moin (1985), relying on the Helmholtz–Hodge decomposition. The prediction step is advanced in time by employing a Taylor scheme for Finite-Volume method of the 4th-order (TFV4A) scheme (Kraushaar, 2011), combining a fourth-order Runge–Kutta scheme with a fourth-order Lax–Wendroff-like scheme. The deflated preconditioned conjugate gradient algorithm is used for the correction step that involves solving a Poisson equation to determine pressure (Moureau *et al.*, 2011; Malandain *et al.*, 2013). The solver has been extensively employed across a wide range of turbulent-flow studies and rigorously validated against experimental data (Zmijanovic *et al.*, 2017; Berthelon *et al.*, 2023), including heat-transfer applications involving impinging jets (Grenouilloux *et al.*, 2021).

The convective time step is fixed using the Courant–Friedrichs–Lewy condition which is set to 0.4. Diffusion is another constraint on the time step; the associated viscous time step is fixed according to the Fourier number, which is set to 0.15.

Droplets are considered within a one-way spherical point-particle formalism that accounts for drag and gravity forces. Drag is modelled with the empirical correlation of Schiller and Naumann (Naumann & Schiller, 1935) for moderate values of the particle Reynolds number. The diameter of the particle evolves due to evaporation, for which the Spalding model is adopted (Spalding, 1950). They are assumed to be made of water, but include a non-volatile fraction that limits their evaporation: the final diameter is 1/3rd of the initial diameter, which corresponds to a non-volatile fraction of 3.7 % (Netz & Eaton, 2020).

The one-way coupling allows us to account for the effect of the fluid velocity, temperature and composition on the droplets dynamics and evaporation, but mass, momentum and energy source terms in the fluid equations are neglected, which is justified by the small number of droplets emitted by the exhalation modes considered here Arpino *et al.*, (2022). Indeed, the number of particles generated during breathing or speaking is of the order of 100–1000 per litre (Asadi *et al.*, 2020; Morawska *et al.*, 2009), most of them being smaller than a few microns in diameter (Bagheri *et al.*, 2023). This yields negligible volume fraction and mass loading (Loth, 2000), which justifies the use of one-way coupling for the momentum. As a first approximation, we also neglect the effect of evaporation on the gas phase, which can delay the evaporation (Chong *et al.*, 2021). The advantage of this approximation is that each droplet can be treated independently and its dynamics does not depend on the other droplets exhaled. As a consequence (i) a large number of droplets can be injected to build statistics and (ii) the droplet size distribution does not matter for the calculation. We thus use a uniform size distribution over the range of interest and describe the dynamics as a function of the size with sufficient statistics. We investigate droplets size between 1

and 60 microns: the dynamics of smaller droplets are assumed to be well described by that of 1-micron droplets, all of them having negligible inertia. In addition, the behaviour of droplets of initial diameter larger than 60 microns can easily be extrapolated from the presented results, as will be shown in § 4.

The interaction with the wall is treated as follows: if the particle displacement is such that it reaches the surface within a time step, the particle is assumed to deposit on the surface and remain where it deposited. We consider that splashing of the droplets does not occur (Yarin, 2006), which is justified by the relatively low inertia of the droplets when reaching the surface (Mundo *et al.*, 1995). In addition, resuspension by the flow itself is not considered.

In addition, massless Lagrangian particles are used to visualise and characterise the air flows released during nasal breathing. As these particles do not have inertia, they are simply displaced by the local flow velocity. The velocity of tracers is determined through the interpolation of the local flow velocity at the tracer position, which is then advanced using a third-order Runge–Kutta scheme. Further details about the modelling of particles are available in the Supplementary Materials.

2.2. Computational domain and meshing

The computational domain is a three-dimensional parallelepiped of dimensions 4 m (width) x 4 m (height) x 5 m (length) in the directions x, y and z, respectively. A human manikin with mouth and nose openings is included in the domain. The face of the manikin is symmetric along the x-axis and directed toward the positive values of the horizontal z-axis. It is positioned in a way such that the jets or puffs may freely develop without interacting with the limits of the domain. Here, y is the vertical direction, pointing upward. In simulations involving the table, the table is sufficiently large to ensure that the flow does not interact with its borders. The horizontal extension of the table is not considered here.

For the numerical grid, a first coarse tetrahedral mesh is generated in the three-dimensional parallelepiped computational domain, with elements of edge size around 10 cm. Then, conformal meshing of the surface is obtained inside the in-house solver, which uses a grid cutting algorithm and a subsequent remeshing with the MMG3D mesh adaptation library (Dapogny et al., 2014) to generate the initial grid (Grenouilloux et al., 2023), which faithfully describes the boundaries. That grid has a grid size of 1 mm close to the face of the manikin and 5 mm and the remaining surfaces, but remains coarse (grid size approximately 10 cm) in the volume, including in the regions where the jets will develop. Due to its coarse grid level in the volume, that initial mesh is too coarse to be used for the flow predictions. It is refined on the fly, during the calculation, in regions where the vorticity norm is higher than a small threshold and where the air composition differs from that of the environment. The MMG3D library is used to adapt the grid (Grenouilloux et al., 2023). In addition, the mesh is never coarsened during the simulation and a maximum gradient of mesh size is imposed to prevent grid discontinuities. The smallest grid size, approximately 0.8 mm, is imposed at the exhalation location. The target grid size then varies spatially to follow the growth of the jet. In addition, the grid is refined near the table's surface (grid size 1 mm) to resolve the boundary layer that develops along it. For the breathing cases for instance, the size of the first element at the table is of the order of 1–3 wall units, depending on the case. This results in final grids ranging from 110 to 170 million elements for breathing simulations, and from 105 to 216 million elements for laughing cases. Snapshots of the grid during the simulations are shown in figure S1 of the Supplementary Materials. To assess mesh convergence, additional simulations for all configurations were conducted using different target grid sizes. The comparisons between results obtained on different grid sizes are presented in figures S3 and S5–S8 of the Supplementary Materials.

2.3. Characteristics of the simulations performed

In this study, we will successively consider nose breathing in § 3 and laughing in § 4. Their characteristics will be discussed in detail in each section, but it proves useful to comment about their common features and differences in the present paragraph. In nose breathing, air flow is exhaled and inhaled periodically

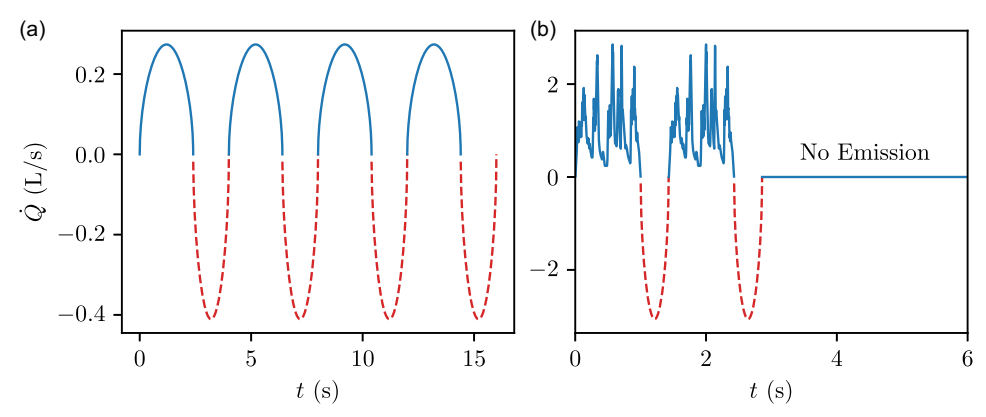


Figure 2. Flow rate signals used in the simulations (solid lines: exhalation; dashed lines: inhalation): (a) first four cycles of the signal for the nasal breathing flow with an exhaled volume of 1 l cycle $^{-1}$. The total duration of the simulations is 80 s, which corresponds to 20 cycles of 4 s, identical to the first four cycles displayed. Half of the flow rate is imposed at each nostril. (b) First 6 s of the flow rate imposed for the laughing flow simulations. The exhalation signal is injected over 2 cycles of 1.5 s each, then the emission is set to zero for the rest of the simulation (between t = 3 and t = 100 s). The exhaled volume is 1 l cycle $^{-1}$.

at the two nostrils of the manikin. The flow rate signal for the case at 1 litre per breath is displayed in figure 2a. For the laughing case, the flow is exhaled (and inhaled) at the mouth of the manikin. It consists in two series of intense exhalations, followed by zero emission for the rest of the simulation, as shown in figure 2b. Although the exhaled volume per cycle is the same for the two signals displayed in figure 2, the peaks in the flow rate for laughing are approximately ten times higher than the maximum flow rate in the nose breathing case. Both the nose breathing and the laughing cases generate downward flows whose interaction with a table will be the subject of §§ 3 and 4.

No-slip (zero velocity) Dirichlet boundary conditions are imposed on the table and the manikin's body. The solid surfaces are modelled as adiabatic and impermeable boundaries, thus there is no mass or heat transfer from/to the air flow and ambient environment. In particular, this applies to the body of the emitter, so that thermal boundary layer effects are neglected, as often performed in computational fluid dynamics (CFD) studies for transport of pathogens. In an unperturbed thermal boundary layer, the velocities are of the order of 10 cm s⁻¹, which is much less than the order of magnitude of the velocities in the jets considered (a few metres per second). Note also that experiments on manikins have shown that the velocities in the thermal convective boundary layer are decreased when the manikin is seated at a table (Licina *et al.*, 2014), the table screening the flow associated with the lower part of the body.

In the simulation, the temperature and relative humidity of the exhaled air has to be imposed. Data from the literature allow us to define the typical ranges for these parameters (Bourouiba et~al., 2014): 30 to 35°C and 85 %–100 %. For the nose breathing, a temperature of 32°C has been used for the exhaled air, to render the heat exchange role of the nose. For the laugh flow, we have used a temperature of 34°C at the mouth exit, which is often chosen in simulations (Chong et~al., 2021). However, the absolute values are only indicative, the important figures being obviously the non-dimensional numbers that quantify the relative effects of the different physics involved which are discussed next. Relative humidity has been set to 90 % in the exhaled air and 50 % in the ambient air, whose temperature is fixed to 25°C. The compositions of exhaled air and ambient air are provided in terms of mass fraction in Table 1.

The different flow configurations considered (breathing or laughing) are both situations in which a warmer flow is exhaled into an ambient flow at rest. In the study of buoyant jets, the inertial and thermal effects can be quantified by the Reynolds number $Re = U_0 D_0 / \nu$ and the densimetric Froude number $Fr = U_0 / \sqrt{g' D_0}$, where U_0 is the jet-exit velocity, D_0 is the hydraulic diameter of a nostril (with $D_0 = \sqrt{4S/\pi}$, and S representing its surface area), ν the kinematic viscosity of air and g' the

Table 1. Characteristics of the exhaled and ambient air: T_{exh} : exhaled air temperature; T_{amb} : Ambient air temperature; RH: relative humidity. Mass fraction of oxygen (Y_{O_2}) , nitrogen (Y_{N_2}) , argon (Y_{Ar}) , water vapor (Y_{H_2O}) and carbon dioxide (Y_{CO_2})

Configuration	Temperature	RH (%)	$Y_{\mathbf{O}_2}$	$Y_{\mathbf{N}_2}$	Y_{Ar}	$Y_{\mathbf{H}_2\mathbf{O}}$	Y_{CO_2}
Breathing	$T_{exh} = 32^{\circ}\text{C}$	90	0.1678	0.7196	0.0123	0.0274	0.0729
	$T_{amb} = 25^{\circ}\text{C}$	50	0.2291	0.7478	0.0127	0.0099	0.0005
Laughing	$T_{exh} = 34^{\circ}\text{C}$	90	0.16721	0.71703	0.01222	0.0309	0.07264
	$T_{amb} = 25^{\circ} \text{C}$	50	0.2291	0.7478	0.0127	0.0099	0.0005

reduced gravity due to the density difference between the jet and the ambient fluid. Additionally, it is useful to introduce a length scale l_m , which represents the transition from jet-like to plume-like motion some distance away from the jet exit

$$l_{m} = M_{0}^{3/4}/B_{0}^{1/2} = D_{0}Fr, \qquad Q_{0} = \frac{\pi D^{2}}{4}U_{0}, \qquad M_{0} = Q_{0}U_{0}$$

$$B_{0} = g'Q_{0}, \qquad g' = g\frac{|\rho_{amb} - \rho_{jet}|}{\rho_{amb}}, \qquad Fr = \frac{U_{0}}{\sqrt{g'D}}, \qquad (1)$$

where M_0 , B_0 are the specific fluxes of momentum and buoyancy at the jet exit, with Q_0 as the volume flux (Fischer *et al.*, 1979). The densities of the jet and ambient air are denoted by ρ_{jet} and ρ_{amb} . In our simulations, the inflow velocity is not constant, so that the time-averaged velocity during injection will be used (Abkarian *et al.*, 2020) as a reference velocity U_0 .

3. Breathing flow

Nose breathing is first considered. Characteristics of human nasal respiration, respiration frequency, exhaled volume and air velocities and direction vary with various factors, such as anatomy, age, posture and physical activity, etc. (Gupta *et al.*, 2010). Here, we do not aim to examine all possible flow conditions, we rather use values that are typical of breathing and explore the effect of some parameters, focusing on the interaction with a horizontal table. We define a 4 s cycle, with an exhalation time of 2.4 s (figure 2a), consistently with the longer exhalation times reported by Gupta *et al.* (2010). While the flow orientation varies according to the shape of the nose and nasal opening, here, we set the jets to be inclined by 45° downwards with respect to the streamwise axis z and by 25° with respect to the symmetry plane (see figure 1a, b). The breathing volume is varied from 0.66 to 2 l per breath, the latter corresponding to a heavy breathing. The flow rates are obtained by multiplying the signal shown in figure 2a of 1 l per breath, by a constant. The hydraulic diameter of each nostril is $D_0 = \sqrt{4S_0/\pi} = 1.23$ cm, with a surface area of $S_0 = 1.18$ cm². Twenty cycles are computed, for a total physical time of 80s simulated.

The exhaled air is at a temperature of 32° C and the relative humidity has been set to 90%. The ambient air is at 25° C with a relative humidity of 50%.

With a total volume of 1 l per breath from the two nostrils, this yields $Re \approx 1450$ and $Fr \approx 25$ at each nostril exit, using the time-averaged bulk velocity. The relevant characteristics of the breathing cases discussed in this paper, obtained by varying the flow rate or the table position, are reported in table 2.

During nose breathing, emitted particles are less than a few microns in diameter and originate from the lower respiratory tract (Bagheri *et al.*, 2023). Their small size makes them readily transported by the exhaled flow and suspended for long times in the surrounding environment (Morawska & Cao, 2020; Netz & Eaton, 2020). The impact of evaporation on their trajectory is negligible. As a consequence, the trajectory of the exhaled particles is determined by the flow itself, which justifies focusing on the jet dynamics. The jet is thus seeded at constant concentration with massless tracer particles, whose dynamics is essentially the same as the small droplets exhaled during nose breathing, allowing us to

Table 2. Characteristics of numerical simulations for breathing flow. The inflow signals are presented in figure 2a. Here, U_0 denotes the mean velocity of the inflow over one cycle of exhalation only; Re and Fr: the mean Reynolds and mean Froude numbers over the exhalation time of one cycle; h_t : the vertical distance of the table to the emitter's nose; l_m : the characteristic length of the buoyant jet; y_{min}/l_m and $z_{0y_{min}}/l_m$: the maximum vertical penetration of the breathing jets and the associated horizontal location, respectively

Case	Q (L Cycle ⁻¹)	$U_{\theta}~(\mathrm{m~s^{-1}})$	Re	Fr	h_t (cm)	l_m (cm)	h_t/l_m	y_{min}/l_m	$z_{@y_{min}}/l_m$
No table -11 breath ^{-1}	1.0	1.780	1449	24.87	-	30.4	-	1.312	1.669
22 cm - 11 breath ⁻¹	1.0	1.780	1449	24.87	22.2	30.4	0.730	0.619	0.748
32 cm - 11 breath ⁻¹	1.0	1.780	1449	24.87	32.2	30.4	1.058	0.896	1.163
$42 \text{ cm} - 11$ breath^{-1}	1.0	1.780	1449	24.87	42.2	30.4	1.387	1.183	1.440
32 cm - 0.66 1 breath^{-1}	0.66	1.187	965	16.56	32.2	20.2	1.591	1.281	1.643
32 cm – 21 breath ⁻¹	2.0	3.563	2899	49.74	32.2	60.8	0.530	0.449	0.532

characterise the cloud generated by the nose breathing over time. A snapshot of the emitted cloud at the end of the 5th cycle is shown in figure 1a,b.

As observed for mouth breathing by Abkarian *et al.* (2020) in cases of periodic exhalations, each breath feeds one exhaled flow whose characteristics are similar to those of constant turbulent jets. In nose breathing, two main negatively buoyant jets (Turner, 1966; Fischer *et al.*, 1979) are formed (one at each nostril), which travel first downwards then lift due to buoyancy effects. Using the residence time of tracers t_r , which denotes the time since their injection, an average trajectory $\vec{X}(t_r)$ of the jets can be calculated as

$$\vec{X}(t_r) = \frac{1}{2N} \sum_{i=1}^{2} \sum_{i}^{N} \vec{x}_{i,j}(t_r),$$
(2)

where $\vec{x}_{i,j}(t_r) = (x, y, z, t_r)$ is the coordinate vector of the *i*th tracer emitted from nostril *j* and *N* is the number of tracers injected at each nostril. The symmetry of the geometry with respect to *x* yields an average trajectory in the (z,y) plane (see figure 1a). We consider particles with injection times t_i ranging from 60 to 80 s to obtain well-converged trajectories from $t_r = 0$ to 25 s, discarding the initial transient phase, which may be particularly long.

The trajectory of the unbounded jet (no table), non-dimensionalised by the length scale $l_m = D_0 Fr$, is shown in figure 3a. The inclined, unbounded jet is initially momentum driven and its trajectory first follows a straight line. As the jet gradually expands in the cross-stream direction, it decelerates due to both the entrainment of the ambient fluid and the opposing buoyancy force. Eventually, the buoyancy overcomes the vertical component of the momentum flux, causing the jet to reach a terminal depth at $y \approx 1.3 l_m$ before going upwards, along a skewed trajectory that is best characterised by a quartic polynomial (Papakonstantis and Christodoulou, 2020, see also figure S2 in the Supplementary Materials). The length scale l_m indeed characterises this transition from jet-like to plume-like motion. For the buoyant jet considered here, the mean value for l_m is found to be approximately 30.4 cm.

We have seen that flows exhaled from nostrils exhibit buoyant jet-like features and may transport particles to a potential interlocutor seated opposite to the emitter. This raises two questions: (i) How do these flows interact with a surface placed beneath the emitter? (ii) What are the consequences of this interaction on forward propagation of the jet and associated droplet transport?

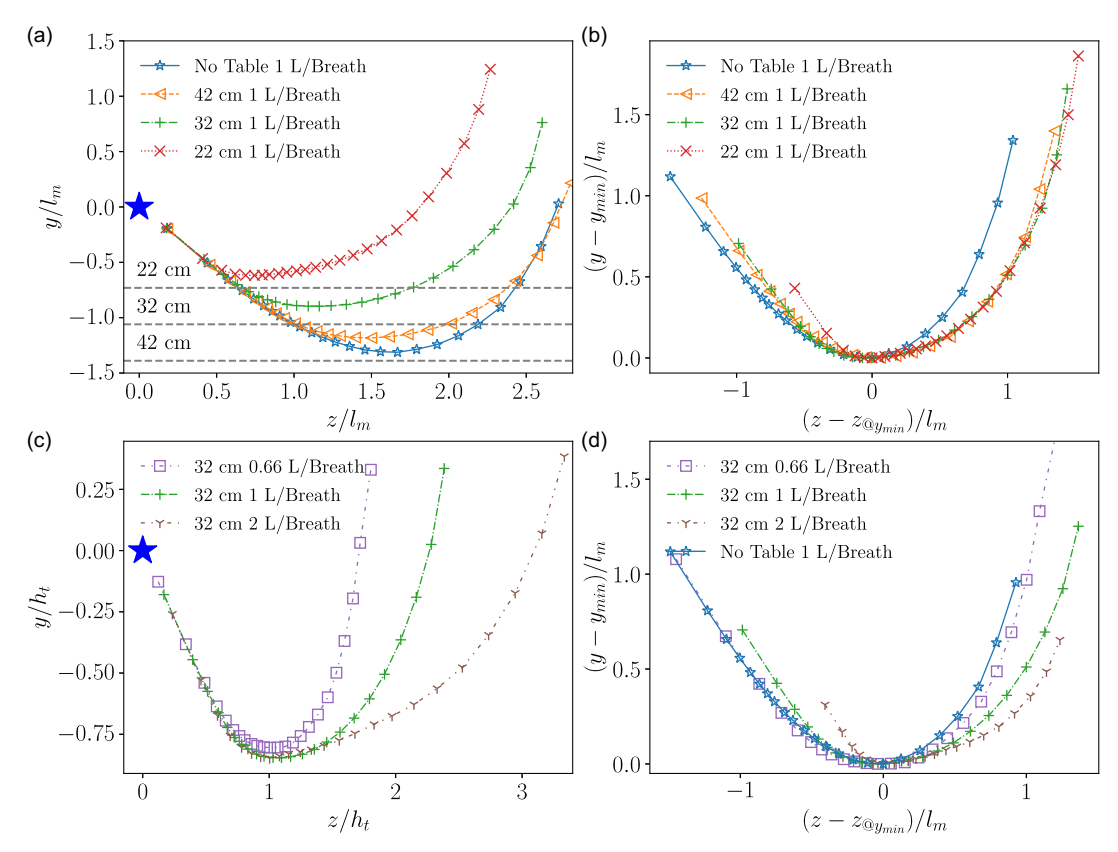


Figure 3. Average trajectories of breathing jets, with different origins and normalisations. (a) Cases with and without the table, for a flow rate of 1 l breath⁻¹ ($Fr \approx 25$, $Re \approx 1450$), normalised by $l_m = D_0 Fr$. Horizontal dashed grey lines show the positions of the tables from the nose of the emitter, denoted by a blue \star , at the origin; (b) same trajectories as in (a) with the origin shifted at the location of minimum height at the jets ($z_{@y_{min}}$; y_{min}); (c) trajectories for cases with the table at $h_t = 32$ cm below the emission, normalised by h_t , for different flow rates; (d) same trajectories as in (c), but normalised by l_m and with the origin shifted at the location of minimum height at the jets ($z_{@y_{min}}$; y_{min}), as in (b); comparison with the case without table at 1 l per breath.

A key point to recall from the rare relevant impinging jet studies is that, depending on the operating conditions – such as jet–wall separation, inclination of the flow and Reynolds number – jets are observed to reach and attach to the surface. Clinging results from a 'Coanda-like effect' in the lower part of the jet, where the presence of the wall restricts the entrainment of ambient air, thereby creating a vertical pressure gradient that maintains the jet along the surface. Sharp & Vyas (1977) explored the conditions that lead to the clinging of a jet (refer to figure 5 in the cited work). In the case just discussed, clinging is estimated to occur for tables placed less than 1.6 l_m (49 cm) lower than the nose. Simulations of the interaction between breathing jets and a horizontal table are presented with three nose–wall separation heights: $h_t = 22$, 32 and 42 cm (which correspond to 0.73 l_m , 1.06 l_m and 1.39 l_m , respectively). Clinging is thus expected for the three cases (Sharp & Vyas, 1977).

In figure 3a, the average trajectories of the 'table jets' are compared with that of the free jet, at Fr = 24.87. Initially, the table jets develop as unbounded jets. Then, the interaction with the table results in the formation of buoyant wall jets (see figure 1a and Supplementary Movie S4). When the table is higher than the terminal height of the free jet trajectory (cases 22 and 32 cm), the jet development is strongly constrained, yielding a shorter penetration in the vertical and the horizontal directions. For lower table heights, the jet—wall interaction is less pronounced. First, the jet trajectory barely differs from the

free jet in the descending region. However, due to clinging, the wall prevents the jet from lifting as in the free jet due to buoyancy forces (Sharp & Vyas, 1977). However, the difference in forward penetration is small.

In order to compare the trajectories of the wall jets, they are plotted with their origin shifted to the location of the minimum vertical position $(z_{@y_{min}};y_{min})$ in figure 3b. The figure clearly shows that the interaction with the table has modified the shape of the trajectory by bending it along the wall. In addition, figure 3b shows that the three wall jet trajectories actually superimpose on the ascending portion, even though the jets have interacted with the table at different distances from the source, and thus different velocities, diameters, Froude numbers: in particular, friction forces are different, as higher velocities are obtained closer to the wall when h_t is small: the decrease in the forward motion is thus not related to viscous friction. We thus observe that the interaction with the table has not modified the balance between forward transport and buoyancy. The table thus limits the forward penetration by making the exhaled jets form a wall jet earlier in their development as the table is moved closer to the injection.

To probe further the effect of exhaled volume on the propagation of breathing clouds, we use simulations for three different exhaled volumes (0.66, 1.0 and 2.01 per breath, corresponding to approximately Fr = 17, 25 and 50, respectively) at constant $h_t = 32$ cm (figure 3c). Contrary to the jets at 1 and 2 l breath⁻¹, which have the same descending portion, the jet with the lowest breathing volume goes up before reaching the table and does not cling. The trajectories of the clinging jets are initially similar, until $z \approx 1.4 h_t$, then they strongly depart in the ascending portion. For the largest breathed volume (21 cycle⁻¹), a notable increase in the near-wall horizontal extent of the jet is observed. In figure 3d, the trajectories are shifted to the location of the minimum vertical position and non-dimensionalised by l_m , as in figure 3b. It is first found that the free jet at 11 breath⁻¹ behaves similarly as the case at 0.66 l breath⁻¹ and the table at 32 cm. As $h_t/l_m = 1.59$ for that case, our results are consistent with the experimental findings of Sharp & Vyas (1977) that clinging should not occur for jets inclined at 45° when the emission-to-surface distance is larger than $h_t/l_m = 1.6$. However, for the clinging jets, the ascending portions of the trajectories do not match, contrary to what was observed in figure 3b. This is consistent with the nonlinear behaviour of cling length with Fr predicted by Sharp & Vyas (1977): contrary to the free jet case, the interaction with the table makes the shape of the trajectory of the table jets dependent on the Froude number.

The nose breathing simulations have thus shown that periodic breathing yields the formation of two negatively buoyant turbulent jets which interact with the table if placed sufficiently close to the emitter. This interaction may limit the downward penetration of the jet, and also modifies its forward penetration. Let us define as z_0 the forward penetration, the distance in the z direction at which the jets come back to the altitude of the emission y=0. For the free jet, the trajectory in figure 3a intersects y=0 at $z_0\approx 2.7\,l_m$, for instance. The results in terms of forward penetration z_0 as a function of the table distance are displayed in figure 4. The results can be interpreted in the following way: for small values of h_t/l_m , the jet is constrained in its descending motion. As it interacts with the table, it forms a wall jet, bent along the table, but with a limited forward penetration compared with the free jet. However, when the table is lower (here, around 1.3 to 1.4 l_m), the table may cling to the table after an unperturbed descending phase, which yields the characteristic bent trajectory without a large effect on the forward penetration.

We now examine how the table may modify the virus intake by comparing the results for $Fr \approx 25$ with different table positions. We aim to quantify the worst-case scenario, in which a susceptible individual is positioned at the location of highest viral exposure. We will assume that virus intake may be modelled by calculating the number of particles passing through a volume located around the receiver's nose, represented as a sphere of radius 5 cm (a volume of 0.5 l approximately). We will assume that the height of the emitter's nose (y=0) is the height at which infectious particles may be inhaled by an interlocutor.

In turbulent jets, the concentration of the discharged material decreases as the inverse of the distance from the emission 1/s. Figure 3a shows that 'table jets' at $h_t = 22$ and 32 cm return to y = 0 by travelling a shorter distance than the free jet. Consequently, if these jets reach a susceptible individual, they would deliver a higher concentration of infectious particles.

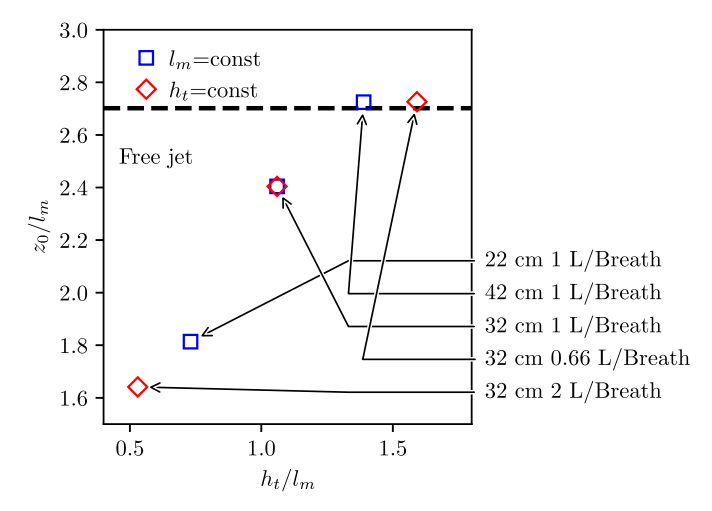


Figure 4. Horizontal penetration of the jets z_0 , measured as the distance at which the average trajectory reaches the emission height y = 0, normalised by l_m . The result for each case is reported as a function of the reduced table distance h_t/l_m . The series with blue squares correspond to the results at constant l_m plotted in figures 3a and 3b. The series with red diamonds correspond to the results at constant h_t plotted in figures 3c and 3d. The horizontal dashed line represents the terminal height of the free jet ('no table -1 l per breath').

We will first consider for each of the two jets of each case at $Fr \approx 25$ (shown in Figure 3a) one sphere placed at the locations where the trajectory of the jet gets back to y = 0, as if evaluating the most adverse placement for each configuration. In order to smooth the results, we add 4 other spheres positioned by displacing the first one by 10 cm (twice the radius) in the -x, +x, -z and +z directions and average the data. For each of the ten spheres (5 spheres per jet and 2 jets), the number of particles entering that sphere is calculated over time as a proxy for virus intake, ten results are averaged, yielding a typical measure of virus intake in the core of the jet. While the quantitative results depend on the spheres' locations and sizes, all of our tests estimating viral intake produce the same overall trends and conclusions. Results are non-dimensionalised by the total number (for the two nostrils) of particles injected per cycle and plotted in figure 5 for all cases at $Fr \approx 25$, without a table and with the three different table positions. First, differences between the free jet and the '42 cm' table jet are small. On the contrary, transmission risks are increased in the '22 cm' and '32 cm' table jets by two effects: first, the time at which the first particles reach the interlocutor's face is smaller than for the free jet; then, the slope of the curves, which informs us about the particle flux, indicates that the local particle concentration opposite to the emitter tends to increase as the table distance is decreased.

In addition, we now discuss the cases of a susceptible person located this time in front of the emitter (x=0), at different distances in the z direction. In the same way, we place fictive spherical probes of 5 cm radius at different positions, right opposite to the emitter: (x=0; y=0; z=55-95 cm). The number of particles entering the spheres is now calculated for each case, and plotted in figure 6. At a given position, the different cases are not ordered the same in terms of virus intake: at z=0.55 and z=0.65 m, the virus intake is significantly larger for the 22-cm case, while at z=0.95 m, the virus intake is much larger for the 42-cm case. The virus intake indeed depends on the forward penetration of the jet, so that the position of the maximum virus intake differs for the different cases: the closer the table, the closer the position at which maximum virus intake is found. In addition, the closer the table, the higher the maximum virus intake: the maximum virus intake is obtained for the 22-cm case (figure 6a), then the 32-cm case (figure 6c), then the 42-cm case (figure 6c). It is also seen that the free jet behaves differently from the others, with lower values on the centreline, which is consistent with the orientation of the jet at the nose exit. Figure 6 also illustrates the time required for the jets to reach a steady state in terms of particle behaviour. In particular, the trajectories of the particle clouds from the first few cycles resemble those

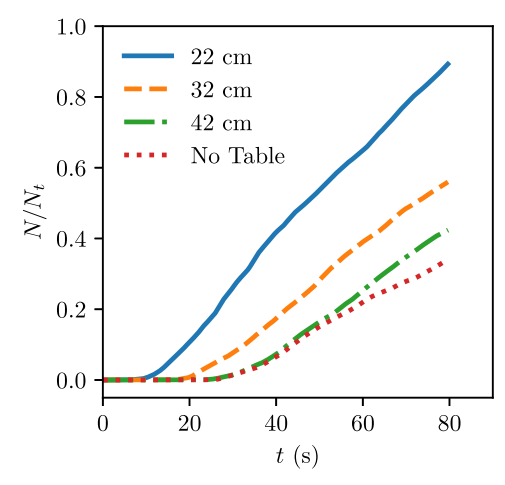


Figure 5. Virus intake over time for the cases at $Fr \approx 25$, with and without a table, for a position of a receiver in the core of the jet, where the trajectory of the jet returns to y = 0. Virus intake is modelled as the number of tracers entering a spherical probe of radius 5 cm at the position of the receiver's nose. The plots are normalised by the number of particles emitted per breath (N_t) , which is the same for the presented cases.

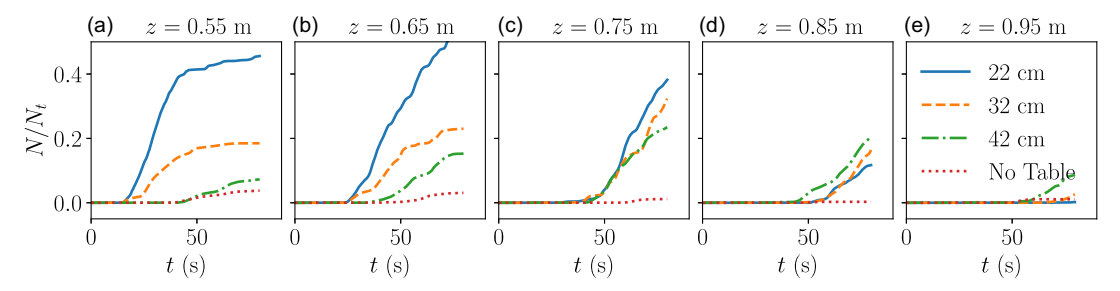


Figure 6. Virus intake over time for the cases at $Fr \approx 25$, with and without a table, for different positions of a receiver in front of the emitter, modelled as the number of tracers entering a spherical probe of radius 5 cm at the position of the receiver's nose: x = 0; y = 0; z = 55 cm (a), z = 65 cm (b), z = 75 cm (c), z = 85 cm (d), z = 95 cm (e). Results are normalised by the number of particles emitted per breath (N_t) .

of isolated puffs rather than a continuous jet, resulting in reduced forward penetration. This transient behaviour accounts for the different slopes observed in the virus intake over time before the system reaches a steady state.

Interestingly, although the virus intake is lower on the centreline than along the jet direction, the orders of magnitude reported in figures 5 and 6 are similar, which show the robustness of the results with respect to the exact position of the receiver.

4. Laughing flow

While breathing flow is characterised by periodic exhalations at moderate Reynolds numbers, some of the human exhalation types are shorter and faster: shout, cough, laughter, sometimes speech, not to mention sneeze. We consider here a signal mimicking laughter, composed of 2 series several short and high-speed exhalations directed downwards (see figure 1c). Laughter indeed generates high-speed downward flows, as illustrated by Bhagat *et al.* (2020), and by an experiment shown in their movie S3 (and figure S10).

An inflow signal of 1.5 s per cycle is considered, with a flow rate profile that captures the intermittent feature of laughing flows with high-frequency bursts generating coalescent puffs: the signal consists of

an exhalation of 1 s with 5 peaks at 2 to $3 \, 1 \, s^{-1}$ and an inhalation of 0.5 s (in practice, a cycle of a signal previously used for speech (Abkarian *et al.*, 2020) is compressed in time and increased in magnitude so that the exhalation lasts 1 s and the exhaled volume per cycle is 1 litre (see figure 2b). Two consecutive cycles are computed. After the 2 cycles of injection, a large puff is formed. The simulation is continued until 100 s without any flow rate at the mouth to isolate the dynamics of the puff.

The flow exits from an elliptic mouth surface of hydraulic diameter $D_0 = 2.46$ cm and is directed downwards, with a 45° angle (figure 1c). The exhaled air has a temperature of $T_{exh} = 34$ °C with relative humidity (RH) of 90 %. The flow is released into a still environment at $T_{exh} = 25$ °C and 50 % RH.

The peak velocity during the injection is approximately 7.1 m s⁻¹ and the average value during injection is approximately 2.34 m s^{-1} . This yields a maximum (respectively average) Reynolds number during the emission of approximately $Re_{max} = 11750$ (respectively Re = 3900). The densimetric Froude number, based on the maximum (respectively average) velocity is $Fr_{max} = 69$ (respectively Fr = 23). The characteristic length of the free flow can be calculated based on the average Froude number: $l_m = D_0 Fr \approx 57$ cm. Particles with initial diameters ranging from 1 to $60 \, \mu m$ (as will be apparent, the dynamics of larger particles can be extrapolated from the simulations) with a uniform distribution are injected at the inflow with an initial velocity equal to that of the gas. These particles are used as a proxy for expiratory droplets and evaporate down to a minimum diameter. As already detailed in § 2.1, thanks to the one-way coupling, the dynamics of the particles is computed without an effect on the flow. Thanks to this assumption, a large number of particles can be injected, and a uniform distribution is used. The objective is to document the fate of droplets as a function of their size. The evolution of the particle cloud is studied in the presence of a horizontal table located 30 cm lower than the person's mouth (figure 1c,d), or without the table. The conditions selected yield $h_t/l_m \approx 0.53$. Supplementary Movie S5 illustrates the dynamics of cloud in the presence of a table.

Figure 7 shows the evolution in time of the particle cloud in both configurations. In the 'no-table' case (b series), the cloud is first dominated by inertia and moves along the direction imposed at the mouth (see figure 7b1). When buoyancy overwhelms the vertical momentum, the cloud is deflected upwards, as shown by the dynamics of the smallest particles. The largest droplets leave the cloud early in the descent stage and are mostly settled out of the cloud during its ascent. As in the breathing flow cases, when a table is placed above the location of the terminal descent of the free jet (a series), the exhaled flow impacts the table (figure 7a1), which cancels its vertical momentum and limits its forward motion. The maximum streamwise distance reached in the 'no-table' configuration is more than 2.5 m, but less than 2 m in the case with the table. A number of particles deposit on the table, which will be analysed further.

To quantify the impact of the table on the particles that may be inhaled by a person located in front of the emitter at different distances, three spherical probes with a radius of 5 cm are placed opposite the emitter at 50, 100 and 150 cm. Their location is displayed in figure 7. Figure 8 shows the histograms of diameters for the particles having entered those spheres during the simulation. At short distances (50 cm, figure 8a), the puff–table interaction does not change the results significantly. The puff passes lower than the location of the sphere. At the distance of 1 m (figure 8b), the differences are pronounced. While the results without the table are similar to those at the previous location, the number of particles having passed through the sphere is an order of magnitude larger. This corresponds to the location where the table puff lifts off the table. In that table case, few particles reach the probe at z = 150 cm (figure 8c). On the contrary, for the free jet, the maximum number of particles gathered is for the 150 cm location. In addition, the free jet carries droplets from all the injected sizes: flow motions counteract sedimentation and transport some of the largest droplets simulated to a height where they may be inhaled. This is not the case for the table jet, for which the number of droplets collected decreases with the initial diameter. In particular, droplets with an initial diameter larger than $50 \, \mu m$ are never found to reach the probes. The deposition of particles on the table is now examined to understand this difference.

Figure 9 shows the proportion of the particles deposited on the table over time for the table case. The particles from the two cycles are separated (first cycle, figure 9a and second cycle, figure 9b) and the time is shifted to the end of each cycle for comparison. The particles are grouped into 4 bins according

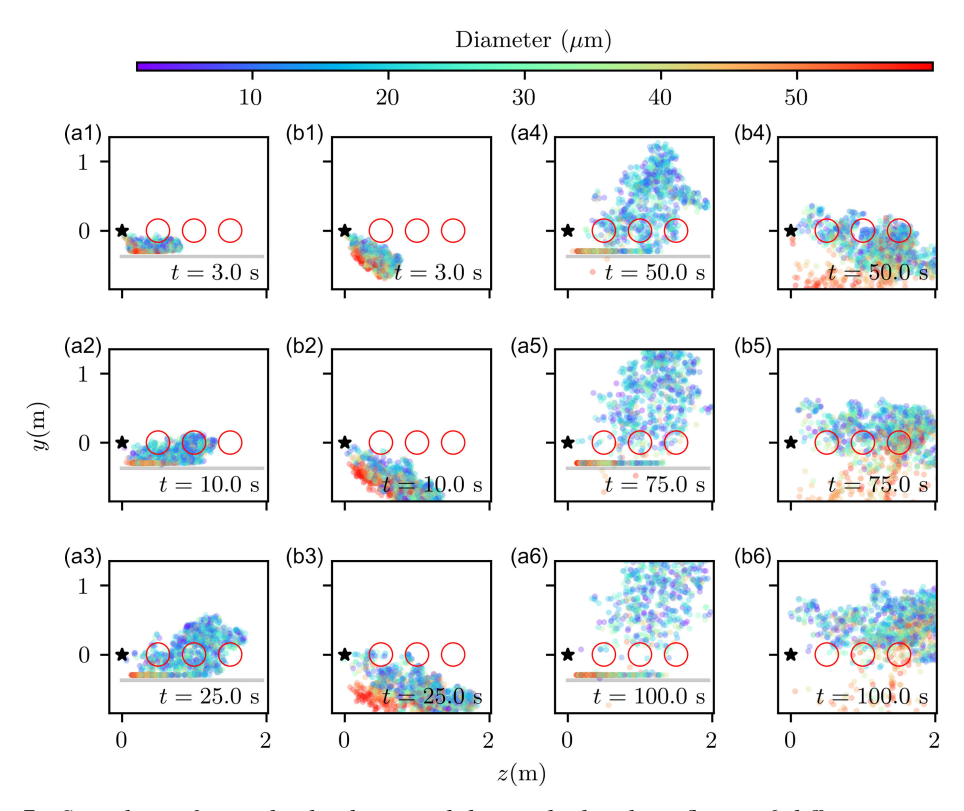


Figure 7. Snapshots of particle clouds emitted during the laughing flow at 6 different time instants: configurations with the table (1st and 3rd column; a1-6) and without the table (2nd and 4th column; b1-6). Each column shows the same configuration. Droplets are coloured by their initial diameter. The \star symbol indicates the mouth of the emitter. Three spherical probes used for evaluating the particle fluxes at the emitter/receiver face height are displayed by \circ . They are located at 50, 100 and 150 cm from the mouth exit and mimic different separation distances between two people seating at a table.

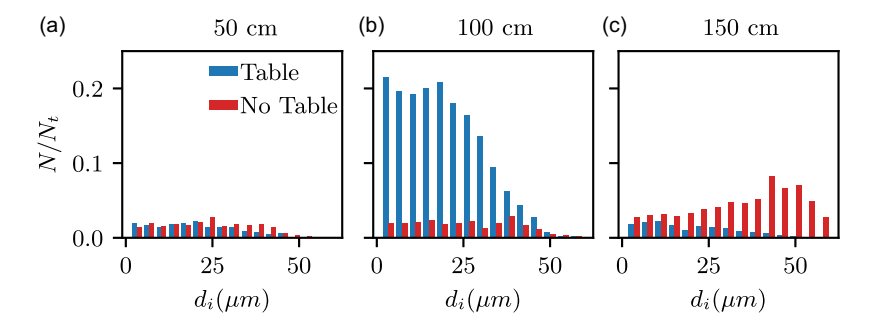


Figure 8. Airborne particles in laughing flow: (a-c) fraction of particles passing through spherical probes centred 50 (a), 100 (b), 150 cm (c) away from the emitter (red circles in figure 7) during the 100 s simulated, as a function of their initial diameter. Here, N_t denotes the total number of particles per bin.

to their initial diameter. First, the proportion of deposited particles increases with their size. More than $90\,\%$ of the emitted particles of initial diameter larger than $45\,\mu m$ are deposited on the table at the end of the simulation, but this ratio drops only to $20\,\%$ for the particles of initial diameter smaller than $30\,\mu m$. In addition, the dynamics is very different: particles within the 30– $60\,\mu m$ range rapidly deposit after the emission, consistently with a rapid deposition at the puff's impact on the table, while the deposition of

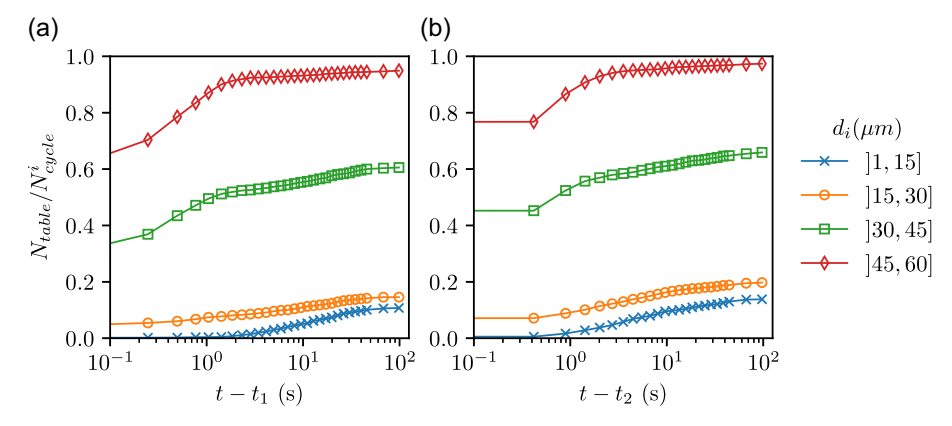


Figure 9. Time evolution of particle deposition on the table for the puffs released during laughter: (a) first cycle; (b) second cycle. Droplets of initial diameter ranging from 1 to 60 μ m are divided into 4 groups, as indicated in the legend. Note that the size distribution of emitted particles is uniform. Here, t denotes the physical time with t_i representing the time of the end of emission of cycle i.

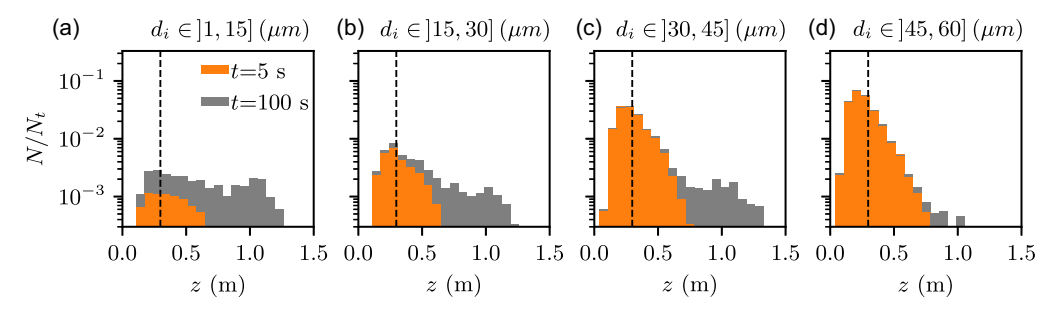


Figure 10. Histogram of particles deposited on the table as a function of the streamwise coordinate z for laughing flow. Approximately $N_t = 33\,000$ particles are injected, with a uniform distribution between 1 and 60 μ m. Particles are grouped into 4 bins based on their initial diameter, i.e. (a) 1–15 μ m, (b) 15–30 μ m, (c) 30–45 μ m, (d) 45–60 μ m. The vertical dashed line represents the streamwise position of the geometric impinging point of the puffs.

the smallest particles is more progressive and characteristic of a slow sedimentation. The differences between the particles of the two cycles is small, but in general, the deposition rate is higher for the second cycle. We interpret this difference as an effect of the second cycle in maintaining the momentum of the particles of the first cycle, slightly limiting their sedimentation compared with those of the second cycle.

In figure 10, we present the density in the z direction of particles deposited over the table, integrated over the spanwise direction x. Particles are grouped into the same 4 bins as in figure 9 and results are plotted at 5 s, soon after the injection is completed, and at 100 s, at the end of the simulation. The maximum deposition of the largest droplets occurs near the geometric stagnation point, which is consistent with the deposition profile in impinging jets with large nozzle-to-surface distances (Burwash et al., 2006). It confirms that the deposition is due to the impact of those particles due to their initial momentum. In contrast, the deposition of smaller particles is more progressive in time and spans over a larger region: it is associated with their sedimentation from the cloud. A peak in the density of small deposited particles is observed below the particle cloud. Figure 10 gathers results from the two cycles simulated, but they are separated in figure S9. Differences between the two cycles are mainly visible for the smallest particles: the particles emitted during the first cycle are pushed further downstream and contribute more significantly to the deposition for $z \ge 0.8$ m.

Overall, the table acts as a filter that collects the largest particles simulated at impact. This has a tremendous effect on the distribution of airborne particles and explains the absence of large airborne particles observed in figure 8 in the table case.

5. Conclusions

We have used LES to explore human expiratory flows and the associated particle transport around a table, to understand short-range airborne transmission from asymptomatic individuals in everyday social interactions, for example, in meetings and restaurants.

Different types of exhalations generate flows directed downwards which, in a colder medium, first have a straight trajectory before being deflected by buoyancy forces. If a table is located above the terminal depth reached by the puffs or jets, it obstructs the vertical penetration of flows and causes them to deviate earlier. While the table shortens the forward propagation of the exhaled material, it also causes the flow to reach a given downstream location sooner after injection. This can result in a higher instantaneous concentration of exhaled material at that location, potentially increasing exposure and transmission risk, should a susceptible individual be positioned at such a distance. We have shown that the presence of a table introduces a new length scale h_t , the distance between the nose/mouth of the emitter and the table, which modifies the free flow dynamics as soon as it is shorter than the terminal penetration of the flow without table. Another important result is that the non-dimensionalised trajectory after the interaction with the table depends on the Froude number, which is not the case without a table, but is independent on the table's position.

Finally, the table modifies not only the trajectory of the exhaled material, but also the content of the exhaled clouds. Indeed the interaction of the flow on the table makes the table an inertial impactor (Marple & Liu, 1974) that collects the largest airborne particles. The table thus introduces a cutoff diameter for the particles able to remain suspended and participate in airborne transmission. As the response of inertial impactors is known to scale as the square root of the particle Stokes number (Marple & Liu, 1974), one expects that the cutoff particle diameter for impaction on the table evolves like the inverse of the square root of the inflow velocity: the faster the exhalation, the smaller the particles remaining in the air after impact. Interestingly, this also allows us to provide new insights into the particles that would participate in the fomite transmission route after deposition on the table's surface.

In our simulations, several assumptions have been made regarding droplet behaviour. Droplet dynamics is modelled using a point-particle Lagrangian approach, and the simulations are one-way coupled. This latter assumption neglects the mass transfer of water from droplets to the gas phase, leading to an overestimation of evaporation rates. In the case of laughing, this likely results in an underestimation of the predicted deposition, both with and without the table. A particularly important yet uncertain aspect concerns the interaction between evaporating respiratory droplets and the table's surface. To the best of our knowledge, such interactions, especially in the late stages of evaporation when most of the water content has been lost (Vejerano & Marr, 2018), have not been thoroughly studied. Consequently, droplets are assumed to deposit upon contact and remain on the surface. Further investigation into the deposition and impact dynamics, as well as the potential resuspension of droplet residues by airflow, is necessary to enhance the accuracy and realism of simulations such as those presented here.

An interesting aspect to investigate would be the effect of the movement of the emitter during the breathing case. In our simulation, the emitter is supposed to be fixed during the simulation, neglecting the natural movements of humans. This certainly reinforces the interaction between the successive puffs and favours jet-like behaviour, limiting the dispersion compared with a case with movements. Investigating the effects of movements would be a study in itself, adding new parameters to the problem (amplitude, frequency and directions of movement). Note, however, that averages of different receiver positions were conducted in estimating the virus intake during breathing, so that our results do not completely depend on the choice of the precise position of possible receiver.

Like most short-range transmission studies (Chong et al., 2021; Abkarian et al., 2020; Wang et al., 2021c), we investigated how an infected individual seeds the immediate surroundings with infectious particles, here, in the presence of a table, and use airborne concentration as a proxy to transmission risk.

The thermal boundary layer (TBL) due to the body temperature of the emitter has been neglected, the exhaled air velocities at the mouth/nose exit being much larger than those in the TBL, in particular in the presence of a table (Licina *et al.*, 2014). On the contrary, it would be necessary to account for the TBL of a susceptible interlocutor (Giri *et al.*, 2022; Singhal *et al.*, 2022) if they were explicitly included in the simulation. Indeed, including a second person in the simulation would be especially interesting in the cases where the emitted flow is sufficiently energetic to travel along the whole table and impact the second body. In that case, we may expect the transport of the airborne particles from the table to the person's face to be influenced by their TBL. Of course, air currents in the rooms associated with heating, ventilation and air conditioning Liu *et al.* (2021); Bhagat *et al.* (2020) may also modify the droplets' fate, and generate interesting interactions with the table and the bodies of the infected and susceptible people.

By demonstrating the complexity of the physical phenomena at play in a relatively simple configuration, our study opens the way to a wide range of possibilities in short-range airborne transmission research. It first highlights the value of investigating more fundamental flow situations, such as the dynamics of impacting turbulent jets and puffs, or unsteady effects in inertial impactors. These situations are not only of intrinsic interest but also provide an opportunity for a thorough validation of LES. Even simplified configurations of buoyant jet–surface interactions, such as buoyant turbulent jets with constant flow rate, could enable more detailed analyses of the turbulent structure and the forces acting on the jet, which were not performed in this study. Such studies would also allow for a broader exploration across parameters like jet angle, Froude and Reynolds number, before introducing pulsatile effects. Such a systematic exploration of the parameter space could also inform simplified, simulation-based models (Wang *et al.*, 2022; Yang *et al.*, 2020) or empirical correlations, offering rule-of-thumb guidelines for practitioners without expertise in fluid mechanics to quantify the effect of the table on the jet penetration, for instance. In addition, our study motivates further work coupling geometry, movements, flow and thermal effects. Overall, we are only at the beginning of the investigation into the effects of geometry settings on the transmission of respiratory diseases.

Supplementary material. Methods section and Supplementary information are available in an additional document. Five Supplementary Movies, cited in the text, are also provided. The supplementary material for this article can be found at https://doi.org/10.1017/flo.2025.10028.

Acknowledgements. The set-up of the CFD simulations was designed with P. Bénard, G. Lartigue, V. Moureau (CORIA, France), G. Balarac, P. Bégou (LEGI, France), Y. Dubief (Univ. Vermont, USA) and R. Mercier (Safran Tech, France).

Data availability statement. Raw data for the graphs, solutions and post-processing scripts are available upon request from the corresponding author (S.M).

Author contributions. O.K, M.A and S.M conceived the research plan and selected the simulation cases. O.K performed the numerical simulations and data analysis. S.M and O.K wrote the manuscript.

Funding statement. This work was funded by the Agence Nationale de la Recherche, project TransporTable (ANR-21-CO15-0002) as well as by the LabEx NUMEV (ANR-10-LABX-0020) under the SATIS project, within the I-Site MUSE (ANR-16-IDEX-0006). The CFD simulations were performed using HPC resources from GENCI-TGCC (Grants No. A0100312498 to A0180312498).

Declaration of interests. The authors declare no conflict of interest.

AI use disclosure. Artificial intelligence tools (specifically Le Chat, ChatGPT) were used on a limited basis for grammar correction, and sentence flow improvements. All outputs were carefully reviewed and revised by the authors, who take full responsibility for the manuscript.

Ethical standards. The research meets all ethical guidelines, including adherence to the legal requirements of the study country.

References

- Abkarian, M., & Stone, H. A. (2020). Stretching and break-up of saliva filaments during speech: A route for pathogen aerosolization and its potential mitigation. *Physical Review Fluids*, 5, 102301.
- Abkarian, M., Mendez, S., Xue, N., Yang, F., & Stone, H. A. (2020). Speech can produce jet-like transport relevant to asymptomatic spreading of virus. *Proceedings of the National Academy of Sciences of the United States of America*, 117(41), 25237–25245.
- Arpino, F., Grossi, G., Cortellessa, G., Mikszewski, A., Morawska, L., Buonanno, G., & Stabile, L. (2022). Risk of sars-cov-2 in a car cabin assessed through 3d cfd simulations. *Indoor Air*, 32(3), e13012.
- Asadi, S., Wexler, A. S., Cappa, C. D., Barreda, S., Bouvier, N. M., & Ristenpart, W. D. (2020). Effect of voicing and articulation manner on aerosol particle emission during human speech. *PLoS One*, *15*(1), e0227699.
- Azimi, P., Keshavarz, Z., Laurent, C., Guillermo, J., Stephens, B., & Allen, J. G. (2021). Mechanistic transmission modeling of COVID-19 on the diamond princess cruise ship demonstrates the importance of aerosol transmission. *Proceedings of the* National Academy of Sciences of the USA, 118(8), e2015482118.
- Bagheri, G., Schlenczek, O., Turco, L., Thiede, B., Stieger, K., Kosub, J. M., Clauberg, S., Pöhlker, M. L., Pöhlker, C., Moláček, J., Scheithauer, S., Bodenschatz, E. (2023). Size, concentration, and origin of human exhaled particles and their dependence on human factors with implications on infection transmission. *Journal of Aerosol Science*, 168, 106102.
- Balachandar, S., Zaleski, S., Soldati, A., Ahmadi, G., & Bourouiba, L. (2020). Host-to-host airborne transmission as a multiphase flow problem for science-based social distance guidelines. *International Journal of Multiphase Flow*, 132, 103439.
- Baxter-King, R., Brown, J. R., Enos, R. D., Naeim, A., & Vavreck, L. (2022). How local partisan context conditions prosocial behaviors: Mask wearing during COVID-19. *Proceedings of the National Academy of Sciences of the USA*, 119(21), e2116311119. 10.1073/pnas.2116311119.
- Baya Toda, H., Cabrit, O., Truffin, K., Bruneaux, G., & Nicoud, F. (2014). Assessment of subgrid-scale models with a large-eddy simulation-dedicated experimental database: The pulsatile impinging jet in turbulent cross-flow. *Physics of Fluids*, 26, 075108.
- Bazant, M. Z., & Bush, J. W. M. (2021). A guideline to limit indoor airborne transmission of COVID-19. *Proceedings of the National Academy of Sciences of the USA*, 118(17), e2018995118.
- Berthelon, T., Sahut, G., Leparoux, J., Balarac, G., Lartigue, G., Bernard, M., Moureau, V., & Métais, O. (2023). Toward the use of les for industrial complex geometries. part ii: Reduce the time-to-solution by using a linearised implicit time advancement. *Journal of Turbulence*, 24(6-7), 311–329.
- Bhagat, R. K., Wykes, M. D., Dalziel, S. B., & Linden, P. F. (2020). Effects of ventilation on the indoor spread of COVID-19. *Journal of Fluid Mechanics*, 903, F1.
- Boulet, L., Bénard, P., Lartigue, G., Moureau, V., Didorally, S., Chauvet, N., & Duchaine, F. (2018). Modeling of conjugate heat transfer in a kerosene/air spray flame used for aeronautical fire resistance tests. Flow, Turbulence and Combustion, 101(2), 579–602.
- Bourouiba, L. (2021). The fluid dynamics of disease transmission. Annual Review of Fluid Mechanics, 53, 473-508.
- Bourouiba, L., Dehandschoewercker, E., & Bush, J. W. M. (2014). Violent expiratory events: On coughing and sneezing. *Journal of Fluid Mechanics*, 745, 537–563.
- Burridge, H. C., & Hunt, G. R. (2017). From free jets to clinging wall jets: The influence of a horizontal boundary on a horizontally forced buoyant jet. *Physical Review Fluids*, 2(2), 023501.
- Burwash, W., Finlay, W., & Matida, E. (2006). Deposition of particles by a confined impinging jet onto a flat surface at Re = 10⁴. *Aerosol Science and Technology*, 40(3), 147–156.
- Carabelli, A. M., Peacock, T. P., Thorne, L. G., Harvey, W. T., Hughes, J., COVID-19 Genomics UK Consortium, Peacock, S. J., Barclay, W. S., de Silva, T. I., Towers, G. J., & Robertson, D. L. (2023). SARS-CoV-2 variant biology: immune escape, transmission and fitness. *Nature Reviews Microbiology*, 21(3), 162–177.
- Chong, K. L., Ng, C. S., Hori, N., Yang, R., Verzicco, R., & Lohse, D. (2021). Extended lifetime of respiratory droplets in a turbulent vapor puff and its implications on airborne disease transmission. *Physical Review Letters*, 126(3), 034502.
- Chorin, A. J. (1968). Numerical solution of the Navier-Stokes equations. *Mathematics of Computation*, 22(104), 745-762.
- Cortellessa, G., Stabile, L., Arpino, F., Faleiros, D. E., van den Bos, W., Morawska, L., & Buonanno, G. (2021). Close proximity risk assessment for SARS-CoV-2 infection. Science of the Total Environment, 794, 148749.
- Crunfli, F., Carregari, V. C., Veras, F. P., Silva, L. S., Nogueira, M. H., Antunes, Aé S. L.ão M., Vendramini, P. H., Valença, A. G. F., Brandão-Teles, C., Zuccoli, Gda S., Reis-de-Oliveira, G., Silva-Costa, L. D.;cia C., Saia-Cereda, Vônica M., Smith, B. J., Codo, A. C., de Souza, G. F., Muraro, Séfanie P., Parise, P. L., Toledo-Teixeira, D. A., Santos de Castro, . D.;caro M., Melo, B. M., Almeida, G. M., Firmino, E. M. S., Paiva, I. M., Silva, B. M. S., Guimarães, R. M., Mendes, N. D., Ludwig, R. D.;ssa L., Ruiz, G. P., Knittel, T. L., Davanzo, G. G., Gerhardt, J. A., Rodrigues, P. D.;cia B., Forato, J., Amorim, M. R., Brunetti, Nália S., Martini, M. C., Benatti, M. D.;ra N., Batah, S. S., Siyuan, L., João, R. B., Aventurato, . D.;talo K., Rabelo de Brito, M., Mendes, M. J., da Costa, B. A., Alvim, M. K. M., da Silva Júnior, Jé R., Damião, L. D.;via L., de Sousa, I. A.;da M. P., da Rocha, E. D., Gonçalves, S. M., Lopes da Silva, L. H., Bettini, V., Campos, B. M., Ludwig, G., Tavares, L. A., Pontelli, M. C., Viana, R. M. M., Martins, R. B., Vieira, A. S., Alves-Filho, Jé C., Arruda, E., Podolsky-Gondim, G. G., Santos, M. V., Neder, L., Damasio, Aé, Rehen, S., Vinolo, M. A.élio R., Munhoz, C. D., Louzada-Junior, P., Oliveira, R. A.; D., Cunha, F. Q., Nakaya, H. I., Mauad, T., Duarte-Neto, A. N., Ferraz da Silva, L. F., Dolhnikoff, M., Saldiva, P. H. N., Farias, A. S., Cendes, F., Moraes-Vieira, P. M. M., Fabro, A. T., Sebollela, A., Proença-Modena, Jé L., Yasuda, C. L., Mori, M. A., Cunha, T. M., Martins-de-Souza, D.

- (2022). Morphological, cellular, and molecular basis of brain infection in COVID-19 patients. *Proceedings of The National Academy of Sciences of The United States of America*, 119(35), e2200960119. 10.1073/pnas.2200960119.
- Dapogny, C., Dobrzynski, C., & Frey, P. (2014). Three-dimensional adaptive domain remeshing, implicit domain meshing, and applications to free and moving boundary problems. *Journal of Computational Physics*, 262, 358–378.
- Ding, S., Lee, J. S., Mohamed, M. A., & Ng, B. F. (2022). Infection risk of SARS-CoV-2 in a dining setting: Deposited droplets and aerosols. *Building and Environment*, 213, 108888.
- Duguid, J. P. (1946). The size and the duration of air-carriage of respiratory droplets and droplet-nuclei. *Epidemiology & Infection*, 44(6), 471–479.
- Edwards, D. A., Ausiello, D., Salzman, J., Devlin, T., Langer, R., Beddingfield, B. J., Fears, A. C., Doyle-Meyers, L. A., Redmann, R. K., Killeen, S. Z., Maness, N. J., Roy, C. J. (2021). Exhaled aerosol increases with COVID-19 infection, age, and obesity. *Proceedings of The National Academy of Sciences of The United States of America*, 118(8), e2021830118. 10.1073/pnas.2021830118.
- Faleiros, D. E., van den, B., Wouter, B., Lorenzo, , & Scarano, F. (2022). TU Delft COVID-app: A tool to democratize CFD simulations for SARS-CoV-2 infection risk analysis. Science of the Total Environment, 826, 154143.
- Fischer, H. B., List, J. E., Koh, C. R., Imberger, J., Koh, R. C. Y., & Brooks, N. H. (1979). *Mixing in inland and coastal waters*. Academic Press.
- Fisher, K. A., Tenforde, M. W., Feldstein, L. R., Lindsell, C. J., Shapiro, N. I., Files, D. C., Gibbs, K. W., Erickson, H. L., Prekker, M. E., Steingrub, J. S., Exline, M. C., Henning, D. J., Wilson, J. G., Brown, S. M., Peltan, I. D., Rice, T. W., Hager, D. N., Ginde, A. A., Talbot, H. K., Casey, J. D., Grijalva, C. G., Flannery, B., Patel, M. M., Self, W. H., McClellan, R., Tan, H.-N., Baughman, A., Grear, B., Wu, M., Mlynarczyk, K., Marzano, L., Plata, Z., Caplan, A., Olson, S. M., Ogokeh, C. E., Smith, E. R., Kim, S. S., Griggs, E. P., Richards, B., Robinson, S., Kim, K., Kassem, A. M., Sciarratta, C. N., Marcet, P. L. (2020). Community and close contact exposures associated with COVID-19 among symptomatic adults over 18 years in 11 outpatient health care facilities United States, July 2020. Morbidity and Mortality Weekly Report, 69(36), 1258.
- Galasso, V., Pons, V., Profeta, P., Becher, M., Brouard, S., & Foucault, M. (2020). Gender differences in COVID-19 attitudes and behavior: Panel evidence from eight countries. *Proceedings of the National Academy of Sciences of the USA*, 117(44), 27285–27291. 10.1073/pnas.2012520117.
- Galmiche, S., Charmet, T., Schaeffer, L., Paireau, J., Grant, R., Chény, O., Von Platen, C., Maurizot, A., Blanc, C., Dinis, A., Martin, S., Omar, F., David, C., Septfons, A., Cauchemez, S., Carrat, F., Mailles, A., Levy-Bruhl, D., & Fontanet, A. (2021). Exposures associated with SARS-CoV-2 infection in France: A nationwide online case-control study. *The Lancet Regional Health Europe*, 7, 100148.
- Gandhi, M., Yokoe, D. S., & Havlir, D. V. (2020). Asymptomatic transmission, the achilles' heel of current strategies to control COVID-19. New England Journal of Medicine, 382(22), 2158–2160.
- Giri, A., Biswas, N., Chase, D. L., Xue, N., Abkarian, M., Mendez, S., Saha, S., & Stone, H. A. (2022). Colliding respiratory jets as a mechanism of air exchange and pathogen transport during conversations. *Journal of Fluid Mechanics*, 930, R1.
- Goldstein, R. J., & Franchett, M. E. (1988). Heat transfer from a flat surface to an oblique impinging jet. *Journal of Heat Transfer*, 110(1), 84–90.
- Grenouilloux, A., Leparoux, J., Moureau, V., Balarac, G., Berthelon, T., Mercier, R., Bernard, M., Bénard, P., Lartigue, L., & Métais, O. (2023). Toward the use of LES for industrial complex geometries. Part I: automatic mesh definition. *Journal of Turbulence*, 24(6-7), 280–310.
- Grenouilloux, A., Moureau, V., Lartigue, G., Bénard, P., & Ferrey, P. (2021). Feature-based mesh adaptation applied to the large eddy simulation of multiple jets impinging on a surface. In: *Proceedings UK heat transfer conference*.
- Gupta, J. K., Lin, C.-H., & Chen, Q. (2009). Flow dynamics and characterization of a cough. *Indoor Air*, 19(6), 517–525.
- Gupta, J. K., Lin, C.-H., & Chen, Q. (2010). Characterizing exhaled airflow from breathing and talking. *Indoor Air*, 20(1), 31–39.
 Howard, J., Huang, A., Li, Z., Tufekci, Z., Zdimal, V., van der Westhuizen, H.-M., von Delft, A., Price, A., Fridman, L., Tang, L.-H., Tang, V., Watson, G. L., Bax, C. E., Shaikh, R., Questier, F., Hernandez, D., Chu, L. F., Ramirez, C. M., Rimoin, A. W. (2021). An evidence review of face masks against COVID-19. *Proceedings of The National Academy of Sciences of The United States of America*, 118(4), e2014564118. 10.1073/pnas.2014564118.
- Johnson, G. R., Morawska, L., Ristovski, Z. D., Hargreaves, M., Mengersen, K., Chao, C. Y. H., Wan, M. P., Li, Y., Xie, X., Katoshevski, D., Corbett, S. (2011). Modality of human expired aerosol size distributions. *Journal of Aerosol Science*, 42(12), 839–851
- Kim, J., & Moin, P. (1985). Application of a fractional-step method to incompressible Navier–Stokes equations. *Journal of Computational Physics*, 59(2), 308–323.
- Kraushaar, M. (2011). Application of the compressible and low-Mach number approaches to Large-Eddy Simulation of turbulent flows in aero-engines. PhD Thesis, Institut National Polytechnique de Toulouse-INPT.
- Licina, D., Pantelic, J., Melikov, A., Sekhar, C., & Tham, K. W. (2014). Experimental investigation of the human convective boundary layer in a quiescent indoor environment. *Building and Environment*, 75, 79–91.
- Liu, H., He, S., Shen, L., & Hong, J. (2021). Simulation-based study of COVID-19 outbreak associated with air-conditioning in a restaurant. *Physics of Fluids*, 33(2).
- Loth, E. (2000). Numerical approaches for motion of dispersed particles, droplets and bubbles. *Progress in Energy and Combustion Science*, 26(3), 161–223.

- Malandain, M., Maheu, N., & Moureau, V. (2013). Optimization of the deflated conjugate gradient algorithm for the solving of elliptic equations on massively parallel machines. *Journal of Computational Physics*, 238, 32–47.
- Marple, V. A., & Liu, B. Y. H. (1974). Characteristics of laminar jet impactors. Environmental Science & Technology, 8(7), 648–654.
- Mendez, S., Garcia, W., & Nicolas, A. (2023). From microscopic droplets to macroscopic crowds: Crossing the scales in models of short-range respiratory disease transmission, with application to COVID-19. Advanced Science, 10(19), 2205255.
- Miller, S. L., Nazaroff, W. W., Jimenez, J. L., Boerstra, A., Buonanno, G., Dancer, S. J., Kurnitski, J., Marr, L. C., Morawska, L., & Noakes, C. (2021). Transmission of SARS-CoV-2 by inhalation of respiratory aerosol in the skagit valley chorale superspreading event. *Indoor Air*, 31, 314–323.
- Mishra, A., Djenidi, L., & Agrawal, A. (2023). Flow characterization in the downhill region of a pulsed oblique round jet. *Physical Review Fluids*, 8(5), 054607.
- Mishra, A., Yadav, H., Djenidi, L., & Agrawal, A. (2020). Experimental study of flow characteristics of an oblique impinging jet. Experiments in Fluids, 61, 1–16.
- Morawska, L. J. G. R., Johnson, G. R., Ristovski, Z. D., Hargreaves, M., Mengersen, K., Corbett, S., Chao, C. Y. H., Li, Y., & Katoshevski, D. (2009). Size distribution and sites of origin of droplets expelled from the human respiratory tract during expiratory activities. *Journal of Aerosol Science*, 40(3), 256–269.
- Morawska, L., & Cao, J. (2020). Airborne transmission of SARS-CoV-2: The world should face the reality. Environment International, 139, 105730.
- Moureau, V., Domingo, P., & Vervisch, L. (2011). Design of a massively parallel CFD code for complex geometries. *Comptes Rendus Mécanique*, 339(2-3), 141–148.
- Mundo, C. H. R., Sommerfeld, M., & Tropea, C. (1995). Droplet-wall collisions: Experimental studies of the deformation and breakup process. *International Journal of Multiphase Flow*, 21(2), 151–173.
- Naumann, Z., & Schiller, L. (1935). A drag coefficient correlation. Z. Ver. Deutsch. Ing, 77(318), e323.
- Netz, R. R., & Eaton, W. A. (2020). Physics of virus transmission by speaking droplets. In: Proceedings of the National Academy of Sciences.
- Nguyen, T., Maher, B., & Hassan, Y. (2020). Flowfield characteristics of a supersonic jet impinging on an inclined surface. *AIAA Journal*, 58(3), 1240–1254.
- Nicoud, F., Chnafa, C., Siguenza, J., Zmijanovic, V., & Mendez, S. (2018). Large-eddy simulation of turbulence in cardiovascular flows. In *Biomedical technology* (pp. 147–167). Springer.
- Nicoud, F., Toda, H. B., Cabrit, O., Bose, S., & Lee, J. (2011). Using singular values to build a subgrid-scale model for large eddy simulations. *Physics of Fluids*, 23(8), 085106.
- Nielsen, P. V., & Xu, C. (2022). Multiple airflow patterns in human microenvironment and the influence on short-distance airborne cross-infection A review. *Indoor and Built Environment*, 31(5), 1161–1175.
- Oran, D. P., & Topol, E. J. (2020). Prevalence of asymptomatic SARS-CoV-2 infection: A narrative review. *Annals of Internal Medicine*, 173(5), 362–367.
- Papakonstantis, I. G., & Christodoulou, G. C. (2020). Simplified modelling of inclined turbulent dense jets. Fluids, 5(4), 204.
- Shao, S., Zhou, D., He, R., Li, J., Zou, S., Mallery, K., Kumar, S., Yang, S., & Hong. Jiarong 2021 risk assessment of airborne transmission of COVID-19 by asymptomatic individuals under different practical settings. *Journal of Aerosol Science*, 151, 105661
- Sharp, J. J., & Vyas, B. D. (1977). The buoyant wall jet. Proceedings of the Institution of Civil Engineers, 63(3), 593-611.
- Singhal, R., Ravichandran, S., Govindarajan, R., & Diwan, S. S. (2022). Virus transmission by aerosol transport during short conversations. Flow, 2, E13.
- Spalding, D. B. (1950). Combustion of liquid fuels. Nature, 165(4187), 160-160.
- Stadnytskyi, V., Bax, C. E., Bax, A., & Anfinrud, P. (2020). The airborne lifetime of small speech droplets and their potential importance in SARS-CoV-2 transmission. *Proceedings of the National Academy of Sciences of the USA*, 117(22), 11875– 11877.
- Tang, J. W., Nicolle, A. D. G., Pantelic, J., Jiang, M., Sekhr, C., Cheong, D. K. W., & Tham, K. W. (2011). Qualitative real-time schlieren and shadowgraph imaging of human exhaled airflows: An aid to aerosol infection control. *PLoS One*, 6(6), e21392.
- Trivedi, S., Gkantonas, S., Mesquita, L. C. C., Iavarone, S., de Oliveira, P. M., & E., Mastorakos. (2021). Estimates of the stochasticity of droplet dispersion by a cough. *Physics of Fluids*, 33(11), 115130. 10.1063/5.0070528/19783412/115130_1_online.pdf.
- Turner, J. S. (1966). Jets and plumes with negative or reversing buoyancy. Journal of Fluid Mechanics, 26(4), 779-792.
- Vejerano, E. P., & Marr, L. C. (2018). Physico-chemical characteristics of evaporating respiratory fluid droplets. *Journal of the Royal Society Interface*, 15(139), 20170939.
- Wang, C. C., Prather, K. A., Sznitman, J., Jimenez, J. L., Lakdawala, S. S., Tufekci, Z., & Marr, L. C. (2021a). Airborne transmission of respiratory viruses. *Science*, 373(6558), eabd9149.
- Wang, E. Y., Mao, T., Klein, J., Dai, Y., Huck, J. D., Jaycox, J. R., Liu, F., Zhou, T., Israelow, B., Wong, P., & et al. (2021b). Diverse functional autoantibodies in patients with COVID-19. *Nature*, 595(7866), 283–288.
- Wang, J., Alipour, M., Soligo, G., Roccon, A., De Paoli, M., Picano, F., & Soldati, A. Short-range exposure to airborne virus transmission and current guidelines. In: *Proceedings of the National Academy of Sciences 118*, (2021c), e2105279118.
- Wang, J., Dalla Barba, F., Roccon, A., Sardina, G., Soldati, A., & Picano, F. (2022). Modelling the direct virus exposure risk associated with respiratory events. *Journal of the Royal Society Interface*, 19(186), 20210819.

- Wells, W. F. (1934). On air-borne infection: Study II. Droplets and droplet nuclei. American Journal of Epidemiology, 20(3), 611-618.
- WHO: Statement on the fifteenth meeting of the IHR. (2005). Emergency committee on the COVID-19 pandemic. Retrived 3 October, 2024 from. https://www.who.int/news/item/05-05-2023-statement-on-the-fifteenth-meeting-of-the-internationalhealth-regulations-(2005)-emergency-committee-regarding-the-coronavirus-disease-(covid-19)-pandemic
- Yang, F., Pahlavan, A. A., Mendez, S., Abkarian, M., & Stone, H. A. (2020). Towards improved social distancing guidelines: Space and time dependence of virus transmission from speech-driven aerosol transport between two individuals. Physical Review Fluids, 5(12), 122501(R).
- Yarin, A. L. (2006). Drop impact dynamics: Splashing, spreading, receding, bouncing. Annual Review of Fluid Mechanics, 38(1), 159-192.
- Zhang, R., Li, Y., Zhang, A. L., Wang, Y., & Molina, M. J. (2020). Identifying airborne transmission as the dominant route for the spread of COVID-19. Proceedings of the National Academy of Sciences of the USA, 117(26), 14857-14863. 10.1073/pnas.2009637117.
- Zmijanovic, V., Mendez, S., Moureau, V., & Nicoud, F. (2017). About the numerical robustness of biomedical benchmark cases: Interlaboratory FDA's idealized medical device. International Journal for Numerical Methods in Biomedical Engineering, 33(1), e02789.

Cite this article: Kaplan O, Abkarian M and Mendez S (2025). How a table modulates the risk of airborne transmission between facing individuals. Flow, 5, E37. https://doi.org/10.1017/flo.2025.10028